Journal of Alloys and Compounds 793 (2019) 695–704

Contents lists available at ScienceDirect

Journal of Alloys and Compounds

journal homepage: http://www.elsevier.com/locate/jalcom

Correlating the optical property evolution in the Au-Ni binary thin films: From metastable solid solution to phase separated alloy

Robyn Collette [a], Yueying Wu [a, b], Philip D. Rack [a, c, *]

[a] Department of Materials Science and Engineering, University of Tennessee, Knoxville, TN 37996, United States
[b] Department of Chemistry and Biochemistry, University of Notre Dame, Notre Dame, IN 46556, United States
[c] Center for Nanophase Materials Science, Oak Ridge National Laboratory, Oak Ridge, TN 37831, United States

ARTICLE INFO

Article history:
Received 28 February 2019
Received in revised form
15 April 2019
Accepted 21 April 2019
Available online 24 April 2019

Keywords:
Combinatorial sputtering
Thin film
Alloy
Plasmonic alloys
Dielectric function model

ABSTRACT

In this study, the optical properties of $Au_{1-x}Ni_x$ alloy thin films are investigated by employing a combinatorial sputtering approach. The dielectric function is measured using spectroscopic ellipsometry and is correlated to the composition, determined by energy dispersive spectroscopy, and phases present, determined via x-ray diffraction. As-deposited alloys form a metastable solid solution, however, annealed alloys exhibited phase separation into Au-rich and Ni-rich phases due to the large miscibility gap in the Au-Ni material system. The optical properties are then rationalized by modeling the dielectric function of the solid solution alloys with a Drude-Critical Point analytical model. Lastly, the efficacy of the model is demonstrated which shows that the dielectric function of the phase separated alloys can be approximated using a composition-weighted average of two solid solution dielectric functions.

1. Introduction

Metallic alloys provide a pathway to tune the plasmonic response of a material [1]. For instance, several Au alloys have been explored for plasmonic applications. Since Au is a noble metal, in some cases, alloying is explored to improve resistance to oxidation or corrosion while maintaining good plasmonic properties [2]. For example, Au-Cd alloys cause a shift in the in the imaginary dielectric constant to different energies than that of pure Au, which increases the losses in one energy range while decreasing losses at other energy regions [3]. Other applications explore alloying to add functionality. More specifically, creating alloys of noble-transition metal components may allow for combination of plasmonic properties from the noble metal and magnetic or catalytic properties from a transition metal [4]. Amendola et al. demonstrated the coexistence of both plasmonic and magnetic properties in $Au_{0.89}Fe_{0.11}$ alloys and suggested promise for applications in magnetic resonance imaging [5]. More recently, Amendola et al. studied Au-Fe nanoalloys with various compositions up to 13 at% Fe addition, demonstrating the surface plasmon resonance exists in this range of alloys albeit decreasing intensity with increasing Fe content [4]. Additionally, Cu-Co [6] and Ag-Co nanoparticles (plasmonic-magnetic, respectively) generated by a pulsed laser induced dewetting process have been studied where phase separated bimetallic nanoparticles evolve from laser melted films; the resultant plasmonic [7] and so-called ferroplasmonic [8] properties have been studied via optical spectroscopy and electron energy loss spectroscopy. The coexistence of magnetic and plasmonic properties has also been shown in the $Au_{1-x}Ni_x$ alloy where $0.02 \leq x \leq 0.10$ [9].

Au and Ni both have a face-centered cubic (FCC) structure. However, Au has a larger lattice parameter (4.08 Å) [10] than Ni (3.52 Å) [11], which causes the alloy system to have limited solubility. The Au-Ni system contains a large miscibility gap in the solid phase region [12] where outside the miscibility gap, Au and Ni form a solid solution. At temperatures below the miscibility gap critical point, 816 °C, Ni has higher solubility in Au while Au has very limited solubility in Ni. Within this miscibility gap, Au and Ni are expected to phase separate into compositions determined by the miscibility gap boundary. For example, at 600 °C the system is expected to phase separate into $Au_{0.78}Ni_{0.22}$ grains and $Au_{0.04}Ni_{0.96}$ grains. Consequently, dewetting of Au-Ni films has been studied where it has been demonstrated that alloying behavior plays a key role in the dewetting process [13].

* Corresponding author. Department of Materials Science and Engineering, University of Tennessee, Knoxville, TN 37996, United States.
E-mail address: prack@utk.edu (P.D. Rack).

https://doi.org/10.1016/j.jallcom.2019.04.207
0925-8388/

Limited optical studies on the full Au-Ni alloy system have been conducted. Bassett et al. studied dilute $Au_{1-x}Ni_x$ alloys where $0.01 \leq x \leq 0.05$. They found that in general, increasing Ni impurities causes enhanced scattering in the energy region below the band edge and a reduced interband absorption above the band edge energy. This results in increased reflectance at lower energy (IR) and a decreased reflectance toward higher energy (UV) [14,15]. More recently, McPherson et al. demonstrated that the dielectric function of Au-Ni thin films can be tuned by changing the electronic configuration of the metastable solid solution, accomplished by varying the stoichiometry. They also demonstrated similar results by stacking Au and Ni films in varying layer numbers and thicknesses [15]. In these cases, only the Au-rich side of the Au-Ni alloy system has been investigated. However, to the best of our knowledge, no study of the dielectric function and annealing effects on the full Au-Ni system has been completed.

We systematically investigate the optical properties of thin film $Au_{1-x}Ni_x$ alloys across the entire phase diagram. The as-deposited material forms metastable solid solutions [15], which, depending on the composition, phase separate upon annealing consistent with the equilibrium phase diagram. The efficacy of the various alloy compositions as a plasmonic material is determined by measuring the dielectric function and calculating the corresponding LSPR quality factor ($-\mathrm{Re}(\varepsilon)/\mathrm{Im}(\varepsilon)$). Furthermore, the optical properties are correlated to the phases present as determined via x-ray diffraction (XRD). While the dielectric function logically changes in the $Au_{1-x}Ni_x$, the dielectric function of the solid solution behaves different than the phase-separated alloys. We rationalize these changes by implementing a Drude-critical point model with three critical points to model the dielectric function with changing composition. Finally, we demonstrate that the model can be applied to model the dielectric function of phase separated alloys by using a composition-weighted average.

There have been a several approaches to modeling the dielectric function of solid solution alloys, Au-Ag for instance Refs. [16,17], as it is well known that an effective medium approximation does not work for solid solutions that are mixed on the atomic scale [18]. For instance, a composition-weighted average model does not accurately predict the varying position of the extinction peak, which varies linearly with composition [19]. Others have tried to rationalize the changes by varying the threshold of interband transitions linearly but failed to take into account changes in the behavior of free electrons with varying composition [20]. The Drude-Lorentz model separates intra- and inter-band effects by using the Drude model to describe the free electron behavior and a certain number of Lorentzian functions to represent interband transitions. However, this model does not always reproduce the data well without adding an arbitrarily large number of Lorentzian terms [21]. A more recent approach that was introduced is the Drude-critical point model, where critical points in the band structure are represented with various functional forms. Etchegoin et al. replaced the Lorentzian terms with critical point terms, which accommodate asymmetric line shapes [21]. This model has realized success in representing the dielectric function of pure Au using only two critical point terms. Rioux et al. used a Drude-critical point model, where the critical point contributions were based on modeling the joint density of states [16]. This model worked well due to the similarity of the Au and Ag band structures and the similar critical point types. Rodriguez compared modeling the dielectric function of Au-Ag alloys using the Drude-Lorentz model with five Lorentzian terms as well as the Drude-critical point model using two critical points [17]. By fitting the dielectric function of individual alloys, he showed that the parameters change with composition in a well-behaved manner. With a description of how the parameters change with composition, the model parameters can be calculated for any Au-Ag alloy composition and used to calculate the complex dielectric function.

It is necessary to have a model to describe the dielectric function behavior in order to accurately simulate, for example, the optical behavior of nanoparticles. For example, Messina et al. simulated the extinction spectra of nanoparticles using published dielectric function data for $Au_{0.85}Ni_{0.15}$ films and compared it to their experimental extinction spectra of $Au_{0.9}Ni_{0.1}$ nanoparticles. They noted that the differences in the simulated and experimental data can be attributed to the difference in compositions [9]. Clearly, having a model to fully describe the system makes it possible to better represent the full composition space.

The Au-Ni system exhibits a dielectric function which changes smoothly with composition. However, a simple composition-weighted average of the pure metal dielectric functions does not reproduce the as-deposited alloy data. Similarly, the Drude-Lorentz model fails to reproduce our data with a reasonable number of Lorentz oscillators (1–5) since it does not accurately account for asymmetric line shapes which reflect more complex joint density of states. The critical point model used by Rioux does also not work well for the Au-Ni system because Au and Ni have dissimilar band structures where certain symmetry points exhibit different critical point characteristics where the transition from one to another is difficult to predict as a function of the $Au_{1-x}Ni_x$ composition. Etchegoin et al. used a Drude-critical point model with two critical points to model the dielectric function of pure Au. It had also been shown that the dielectric function of Ni was well represented using three interband terms [22]. We found this D-CP model, with an additional critical point, fits our data accurately. Thus we model the dielectric function of each solid solution using the Drude-critical point model to rationalize the optical property changes. We utilize three critical points and demonstrate a logical shift in parameters with composition, which effectively allows us to calculate the dielectric function of any Au-Ni solid solution. Using this model, it was then possible to approximate the dielectric function of the phase separated materials using a simple composition-weighted average based on volume fractions.

2. Experimental procedures

2.1. Sample preparation

$Au_{1-x}Ni_x$ films ~300 nm thick were deposited via RF magnetron sputtering onto three 20 mm × 100 mm substrates. The substrates were polished [100] silicon with 100 nm of thermally grown SiO_2. Alloys were formed by co-sputtering pure Au and Ni elemental targets, confocally directed towards the substrate [23]. The chamber was evacuated to below 1×10^{-6} Torr. Sputtering was carried out in an Ar atmosphere at 5 mTorr. Sputtering parameters are listed in Table 1. The sample was oriented to have one end above the Au target and the other above the Ni target, thus achieving a compositional gradient across the long axis of the sample with one end being Au-rich and the other being Ni-rich. One sample was analyzed in the as-deposited state, while two other samples were annealed under vacuum ($<1 \times 10^{-6}$ Torr) for 1 h at 300 °C and 600 °C, respectively.

A second set of samples with a uniform composition of $Au_{0.35}Ni_{0.65}$ was deposited onto seven 30 mm × 30 mm substrates. To achieve uniform composition, the substrate holder was rotated during deposition at 20 RPM. One sample measured in the as-deposited state while the remaining 6 were annealed at 150, 300, 450, 600, 725, and 775 °C, respectively. A third set of isocompositional $Au_{0.28}Ni_{0.72}$ samples were also prepared where one sample was left in the as-deposited state while the others were annealed at 300 °C for 0.5, 1, 2, 3, 5, and 10 h.

Table 1
Sputter deposition parameters.

Composition	Target Power (W)		Stage Rotation (RPM)	Deposition Time (hr:min)	Approximate Deposition Rate (nm/min)
	Au	Ni			
Pure Au	40	0	20	2:00	5.2
Pure Ni	0	110	20	2:00	2.8
$0 < x < 0.3$	40	70	0	0:58	7.7
$0.3 < x < 0.9$	20	110	0	1:30	5.0
$Au_{0.35}Ni_{0.65}$	20	100	20	1:15	5.0
$Au_{0.28}Ni_{0.72}$	20	100	20	1:15	5.0

2.2. Composition measurement and SEM imaging

The film composition at each measurement location was determined using an energy dispersive spectrometer (Bruker) within a scanning electron microscope (Zeiss Merlin). Images were acquired using the in-lens detector at various magnifications. The accelerating voltage was set to 15 kV. Spectra were recorded in an approximately 5 μm × 5 μm area for 60 s. Quantification was performed using the Au Mα peak at 2.123 eV and the Ni Kα peak at 7.480 eV. It was determined that a roughly linear composition gradient of 0.0059 and 0.0077 Δx_{Ni} per mm was achieved (see Fig. 1 for details) for $x < 0.3$ and $0.3 < x < 0.9$ samples, respectively.

2.3. Phase identification

X-ray diffraction and subsequent phase identification for the first set of samples was performed using grazing incidence x-ray diffraction within a 4 mm × 9 mm region, where the composition gradient is in the 4 mm axis and uniform in the 9 mm direction. Consequently, each measurement location has <0.0308 change in composition, x_{Ni}, within the measurement spot size. The incidence angle was set to 4° for these samples and the diffracted beam intensity was recorded from 35° to 55°, a range sufficient to observe the (111) and (200) reflections for Au and Ni. In the second set of samples, the incidence angle was set to 21° to maximize the diffracted beam intensity collected. The data were collected again in the range of 35° to 55°.

2.4. Dielectric function measurement

The complex dielectric function was measured via a J.A. Woolam M-2000U variable-angle spectroscopic ellipsometer in the range of 1.24–5.06 eV. The angle was fixed at 65° and the spot size was 4 mm × 8 mm. Again, the change in composition over the 4 mm spot size is less than 0.0308 x_{Ni}. The alloy films are optically thick and optically smooth, which enables the utilization of a point-by-point fitting of the experimental data to produce Re(ε) and Im(ε). Due to no dispersion model existing that was well suited for our films, no model was used to fit the results.

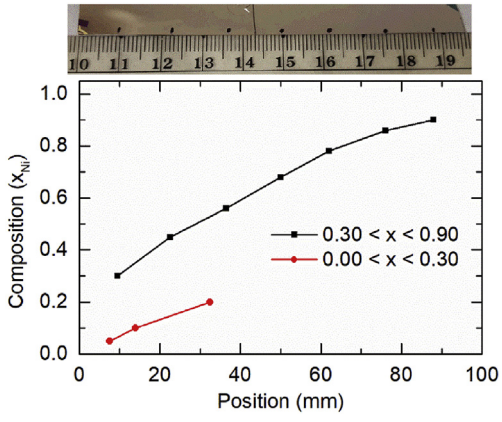

Fig. 1. EDS measured composition versus position demonstrating composition gradient across sample.

2.5. Dielectric function analytical model

The Drude-critical point model described in Etchegoin et al. was used with three critical points (D-3CP):

$$\varepsilon(\omega) = \varepsilon_\infty - \frac{\omega_p^2}{\omega^2 + iG_p\omega} + \sum_{j=1}^{3} A_j \left[\frac{e^{i\phi_j}}{\omega_j - \omega - iG_j} + \frac{e^{-i\phi_j}}{\omega_j + \omega + iG_j} \right] \quad (1)$$

Where the Drude contribution is described by ε_∞, the high-frequency limit dielectric constant, ω_p, the plasma frequency, and G_p, a damping term. The three critical point transitions are each described by an amplitude (A_j), phase (ϕ_j), gap energy (ω_j), and broadening term (G_j). The phase term has a cyclic behavior and repeats every 2π as demonstrated in Fig. S1. In total, there are 15 parameters to describe each composition.

The objective function was selected to be the chi-squared distribution function [17]:

$$f = \frac{1}{2N} \sum_{i=1}^{N} \left[\frac{(\mathrm{Re}_c(\omega_i) - \mathrm{Re}_e(\omega_i))^2}{|\mathrm{Re}_e(\omega_i)|} + \frac{(\mathrm{Im}_c(\omega_i) - \mathrm{Im}_e(\omega_i))^2}{|\mathrm{Im}_e(\omega_i)|} \right] \quad (2)$$

Where N is the number of data points, $\mathrm{Re}_c(\omega)$ and $\mathrm{Im}_c(\omega)$ are the calculated dielectric function components, and $\mathrm{Re}_e(\omega)$ and $\mathrm{Im}_e(\omega)$ are the experimental dielectric function components. For fitting, we employ the built-in *Matlab* algorithm, *GlobalSearch*, using the *fmincon* algorithm. In short, *GlobalSearch* is an efficient search tool to find the global error minimum of a problem by running the fmincon algorithm several times from various starting points within the boundary conditions. Similar to Rioux, we allow each of the 15 parameters to vary quadratically with composition [16]:

$$\omega_p^{x_{Ni}} = a + b(x_{Ni}) + c\left(x_{Ni}{}^2\right) \quad (3)$$

Where x_{Ni} is the atomic Ni fraction, and a, b, and c are the constant, linear, and quadratic coefficients respectively. The optimization routine simultaneously fits all 12 experimental composition data sets and varies the coefficients to minimize the objective function. In total, there are 45 parameters (3 coefficients x 15 model parameters) needed to fully describe the system.

To model the annealed samples that exhibited phase separation, we utilized a simple composition-weighted average of dielectric functions based on the volume fractions of the Au- and Ni-rich phases. Vegard's Law and the Au-Rich (111) and Ni-Rich (111)

peak position from the XRD data was used to determine the approximate phase composition of the two primary phases. The volume fraction of each phase is then determined using the lever rule with the compositions found above. Using our D-3CP model, we calculate the dielectric function of the Au- and Ni-rich phases. Lastly, we use a simple composition-weighted average of the two dielectric functions based on the volume fraction of the two phases to model the effective dielectric function of the annealed samples.

$$\varepsilon(\omega) = \varepsilon_{Au-rich}(1 - x_{Ni}) + \varepsilon_{Ni-Rich}(x_{Ni}) \quad (4)$$

3. Results and discussion

3.1. Full compositional range study

The as-deposited films form a metastable solid solution, and each exhibited 2 main reflections in GIXRD experiments that were characteristic of an FCC crystal structure. As the amount of Ni increased, reflections shift to higher 2θ consistent with the change in the lattice parameter as can be seen in Fig. 2, the reflections shift from that of pure Au toward that of Ni. The shift is approximately linear and follows Vegard's law (Fig. S2). Between x = 0.45 and 0.96, the main (111) peak is broadened and, in some cases, appears to be a combination of two super saturated solid solution peaks.

The as-deposited films exhibited a fairly continuous shift in the dielectric constant as the concentration varied from pure gold to pure nickel. At energies above 2.5 eV, gold has a less negative Re(ε), whereas below this energy gold has a very large negative value which is consistent with its low energy plasmonic behavior. Starting from pure gold, small additions of nickel severely decreases the magnitude of the real part of the dielectric constant. The $Au_{0.14}Ni_{0.86}$ alloy data is in good agreement with that of $Au_{0.15}Ni_{0.85}$ that was previously reported [15]. While in general Im(ε) also shifts almost continuously from pure gold to pure nickel with increasing nickel concentration, in one composition region a discontinuity exists in the values near the 2 eV range, as will be discussed below. As a measure of the suitability of the alloys for plasmonic materials, the peak in the LSPR quality factor, Q-factor, around 1.8 eV is greatly damped compared to that of pure Au (~22). Interestingly, the peak maximum demonstrates a nearly linear shift to higher energy with increasing Ni fraction, but the intensity of the peak decreases exponentially as observed in the inset of Fig. 3g.

In order to rationalize the changes in the dielectric function with composition, we model each composition's dielectric function with a Drude-three critical point (D-3CP) model and observe how the model parameters change with composition. The parameters and fit values for each composition are summarized in Table S1. For example, the total fit and individual components of the fit are plotted for the real and imaginary components of the dielectric function for the $Au_{0.42}Ni_{0.58}$ alloy in Fig. 4a and Fig. 4b, respectively. The parameter trends for energy (ω) and broadening (G) are shown in Fig. 4c and d; the amplitude and phase parameters are shown in Fig. S3. The parameters all exhibit a quadratic behavior with composition. The coefficients governing the behavior are tabulated in Table 2. Some energy parameters were forced to be negative in order to produce a smooth trend. However, the solution is not unique: for instance, the sign of the energy can be positive by subtracting π from the value of ϕ and multiplying the value by −1. We, however, allow these values to evolve as shown so that a smooth parameter trend is produced such that we may use the trend to predict the dielectric function of other alloys.

Subsequent to annealing at 300 °C, some phase separation into an Au-rich phase and a Ni-rich phase occurs as demonstrated in Fig. S4. Based on the phase diagram, these phases should be approximately $Au_{0.98}Ni_{0.02}$ and $Au_{0.005}Ni_{0.995}$, respectively. GIXRD reveals 4 main reflections for each composition. The Au-rich (111) peak is located at slightly higher 2θ than pure Au (111) and is approximately constant for each alloy. A slight shift to lower 2θ in the Ni-rich reflections also occurs consistent with gold alloying. By applying Vegard's law, we can use the Au-rich (111) and Ni-rich (111) reflection positions to approximate the composition. Contrary to the equilibrium values, the XRD results suggest an Au-rich composition of $Au_{0.89}Ni_{0.11}$ and the Ni-rich composition of

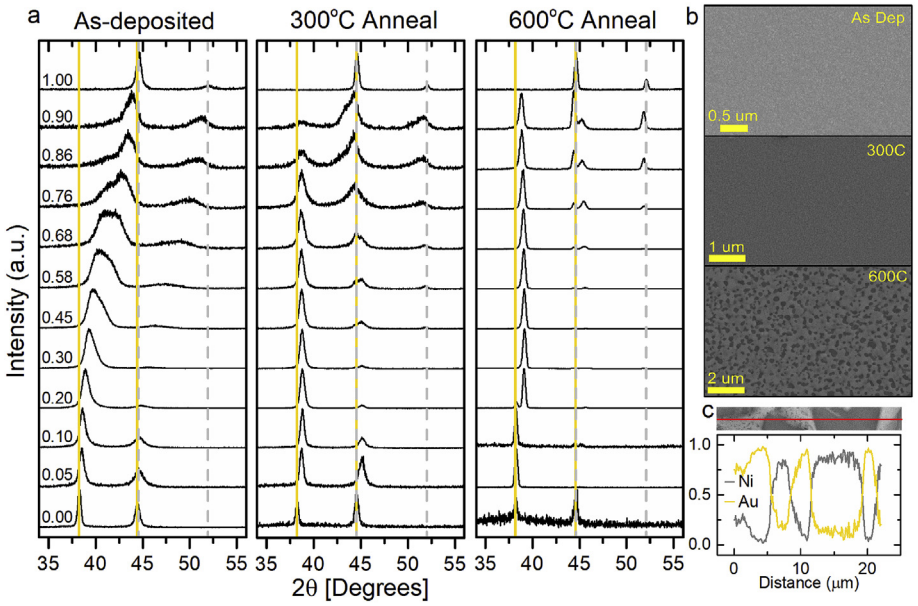

Fig. 2. (a) GIXRD spectra for various $Au_{1-x}Ni_x$ alloy compositions and anneal treatments. Gold lines correspond to measured pure Au (111) and (200) reflections and Gray dashed lines correspond to measured Ni (111) and (200) reflections. (b) SEM images of $Au_{0.42}Ni_{0.58}$ alloy at each anneal condition. (c) EDS line scan with normalized counts demonstrating SEM images are phase contrasted with lighter regions corresponding to Au-rich composition and darker regions corresponding to Ni-rich composition. (For interpretation of the references to colour in this figure legend, the reader is referred to the Web version of this article.)

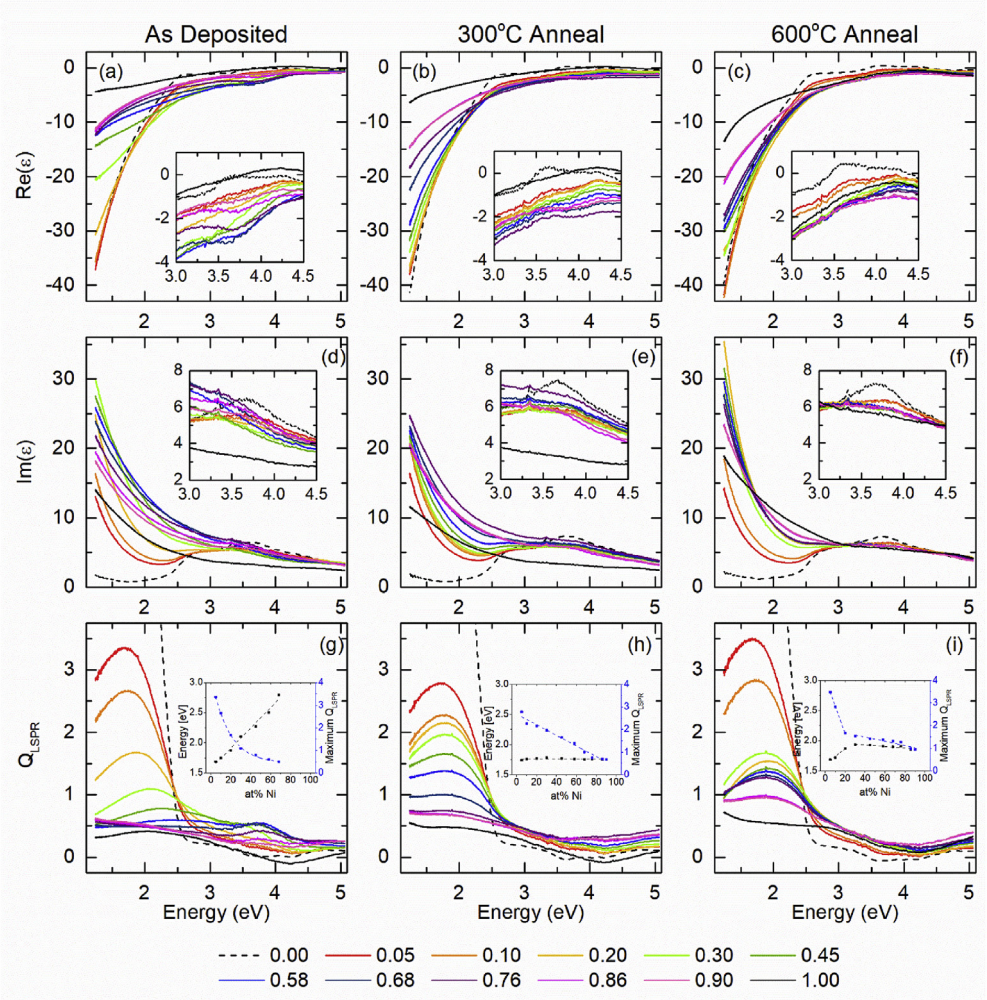

Fig. 3. Real (a–c) and imaginary (d–f) components of the dielectric function and corresponding LSPR Q-factors (g–i) for various $Au_{1-x}Ni_x$ alloys with x indicated in the legend.

$Au_{0.012}Ni_{0.988}$.

Similar behavior to the as-deposited sample is observed in the real and imaginary parts of the dielectric function for the 300 °C annealed sample. However, the feature around 1.8 eV in the Q-factor does not shift with composition like it does in the as-deposited sample. The intensity decreases nearly linearly with increasing Ni content as demonstrated in Fig. 3h. We attribute this to the fact that according to the equilibrium phase diagram, the sample phase separates into two phases; as most of the phases are inside the miscibility gap, the phases are the same as evidenced by constant reflections in the XRD patterns. Rather than the composition systematically changing in the as-deposited sample, the ratio of Au-rich phase to Ni-rich phase simply varies with the change in composition for the 300 °C anneal sample. The compositions with higher Au content contain a higher volume fraction of the Au-rich phase and thus have a higher Q-factor and vice versa.

In order to rationalize the changes in the dielectric function, we employ a simple composition-weighted average of an $Au_{0.89}Ni_{0.11}$ alloy (Au-rich phase) and $Au_{0.012}Ni_{0.988}$ (Ni-rich phase), which are determined using the parameter trends discussed above. The volume fractions are tabulated in Table S2. Fig. 4e demonstrates the fit for the $Au_{0.42}Ni_{0.58}$ alloy and the remaining compositions are shown in Fig. S5. Our model works fairly well for approximating the dielectric function of the alloyed films although the value is not accurate in all cases. We attribute the differences to grain size and surface roughness, which are not accounted for in our model [24].

At higher temperature, we have a larger solid solution range on the Au side of the phase diagram. At 600C, Ni has a higher solubility in Au and consequently we pick up a solid solution behavior in the $Au_{0.93}Ni_{0.07}$ and $Au_{0.90}Ni_{0.10}$ alloys. For compositions where $x > 0.30$, annealed at 600 °C, again the solid solution phase separates as evidenced by the Au-rich and Ni-rich peaks in the GIXRD pattern in Fig. 2; notably the peaks are narrower indicative of larger grains as confirmed by the SEM images (Fig. S4). At 600 °C, in the range of $0.3 \leq x \leq 0.9$, the phase diagram suggests the alloy separates into an $Au_{0.78}Ni_{0.22}$ Au-rich phase and an $Au_{0.04}Ni_{0.96}$ Ni-rich phase. Once again, we apply Vegard's law to the Au-rich and Ni-rich (111) reflections and determined that the Au-rich composition is approximately $Au_{0.88}Ni_{0.12}$ and the Ni-rich composition is approximately $Au_{0.002}Ni_{0.998}$, which are both higher than expected. We attribute this difference to the relatively slow cooling rate of our substrate heater (~16 °C/min). According to the phase diagram at 600 °C and below $x = 0.22$, the resultant microstructure should be a single-phase solid solution. Interestingly, the $Au_{0.2}Ni_{0.8}$ alloy measured at room temperature does have its main GIXRD peak at the approximate solid solution composition, however, there does appear to be an Au reflection thus some gold precipitation occurs during the cooling to room temperature. Annealing at 600 °C is very close to the boundary of the miscibility gap on the phase diagram at this composition.

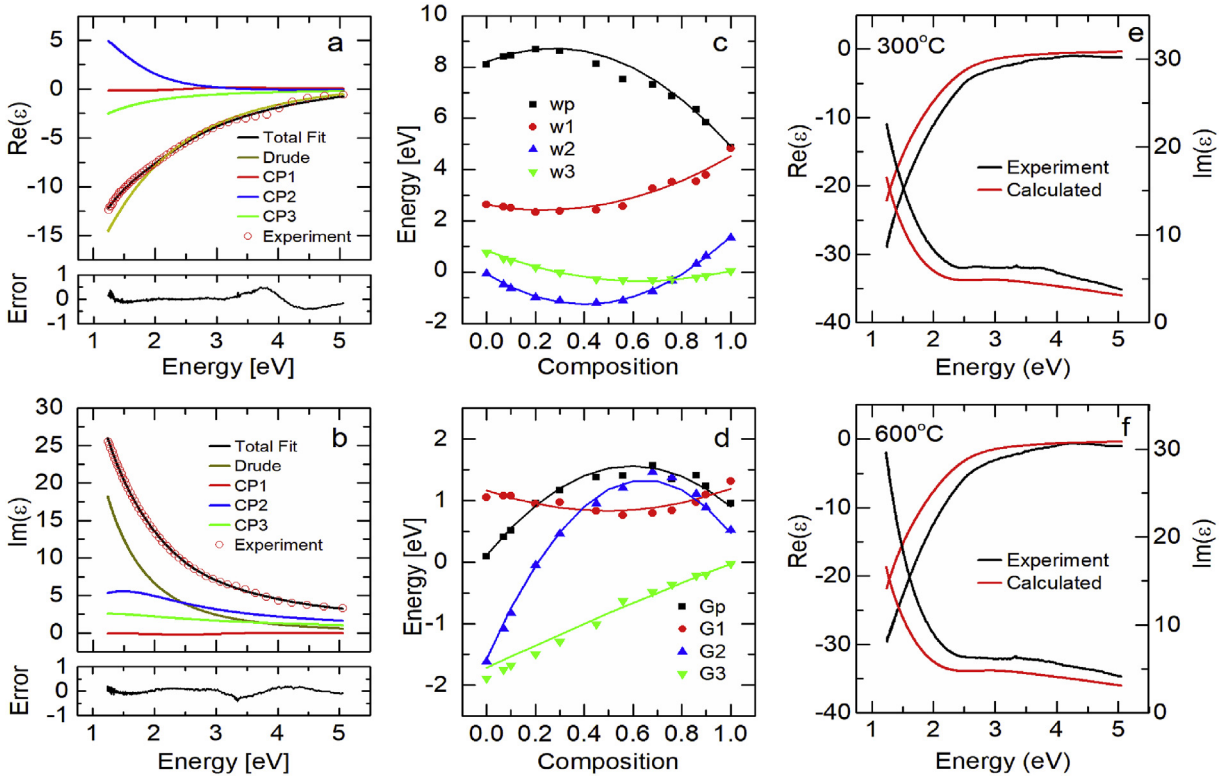

Fig. 4. (Left) (a–b) Total fit using Drude-3CP model and four fit components which make up the total fit for the $Au_{0.42}Ni_{0.58}$ as-deposited alloy. Error plot shows fit-experiment versus energy. (Middle) Energy (c) and broadening (d) parameters versus composition, x, for $Au_{1-x}Ni_x$ alloys. (Right) Experimental (black) and calculated (red) complex dielectric function for an $Au_{0.42}Ni_{0.58}$ alloy after annealing at 300 °C (e) and 600 °C (f). (For interpretation of the references to colour in this figure legend, the reader is referred to the Web version of this article.)

Table 2
Drude-3CP coefficients, a, b, and c, describing quadratic behavior of each parameter. To determine the parameter of a given coefficient, use $a + bx_{Ni} + cx_{Ni}^2$.

	a	b	c
ε_∞	1.994	−0.318	−0.730
ωp	8.196	3.943	−7.218
Gp	0.110	4.863	−4.066
A1	7.529	−17.668	8.765
ϕ1	−1.246	−3.346	1.668
ω1	2.631	−1.733	3.634
G1	1.169	−1.359	1.384
A2	−6.688	42.094	−34.147
ϕ2	−1.591	−4.697	5.637
ω2	−0.057	−5.921	7.363
G2	−1.573	8.966	−6.917
A3	7.605	−38.201	56.981
ϕ3	−1.532	−2.816	1.312
ω3	0.842	−3.731	2.940
G3	−1.718	1.860	−0.170

Because of the extended solid solution, these materials require us to use the D-3CP modeled results in the solid solution region and then an effective medium approximation for compositions within the miscibility gap which exhibited phase separation. We rationalize the change in the dielectric function using the composition-weighted average this time with an $Au_{0.88}Ni_{0.12}$ alloy and an $Au_{0.002}Ni_{0.998}$ alloy. We only apply this to compositions where $x \geq 0.3$ as these compositions are in the miscibility gap and experience phase separation. The calculated and experimental dielectric function for the $Au_{0.42}Ni_{0.58}$ 600 °C alloy is shown in Fig. 4f and the remaining experimental compositions are shown in Fig. S6. In regard to the LSPR Q-factor, the peak shifts to higher energies for the first 3 compositions (x = 0.05, 0.1, and 0.2) consistent with the Au-Ni solid solution that exists in this region as confirmed by XRD. For the rest of the compositions annealed at 600 °C, the maximum in the Q-factor decreases in intensity nearly linearly (but less steep than the 300 °C samples) and the peak maximum remains approximately constant but shifted to higher energy relative to the 300 °C sample. This trend is expected due to the Au-rich phase in the 600 °C annealed samples having more Ni than that of the 300 °C samples.

3.2. $Au_{0.35}Ni_{0.65}$ anneal temperature dependence study

To study how temperature affects the phase evolution and grain size we performed an annealing study on the $Au_{0.35}Ni_{0.65}$ composition, a composition near the maximum in the miscibility gap. The annealing temperature should dictate the phase compositions and subsequent phase fractions. For example, at lower annealing temperature, we expect the alloy to phase separate into nearly pure Au and pure Ni because of the limited solubility; whereas at a higher temperature the phases will contain higher solute concentrations in both the Au- and Ni-rich phases.

XRD patterns for samples annealed at various temperatures (all 1 h) are shown in Fig. 5a. The as-deposited film is again a solid solution as discussed above. The film annealed at 150 °C is also a solid solution and thus we infer the annealing time at this temperature was not sufficient to induce the phase separation in the film. This is evidenced by no shift in the XRD peaks, a very similar dielectric function to the as-deposited film, and no noticeable contrast or grain growth in the SEM image. The

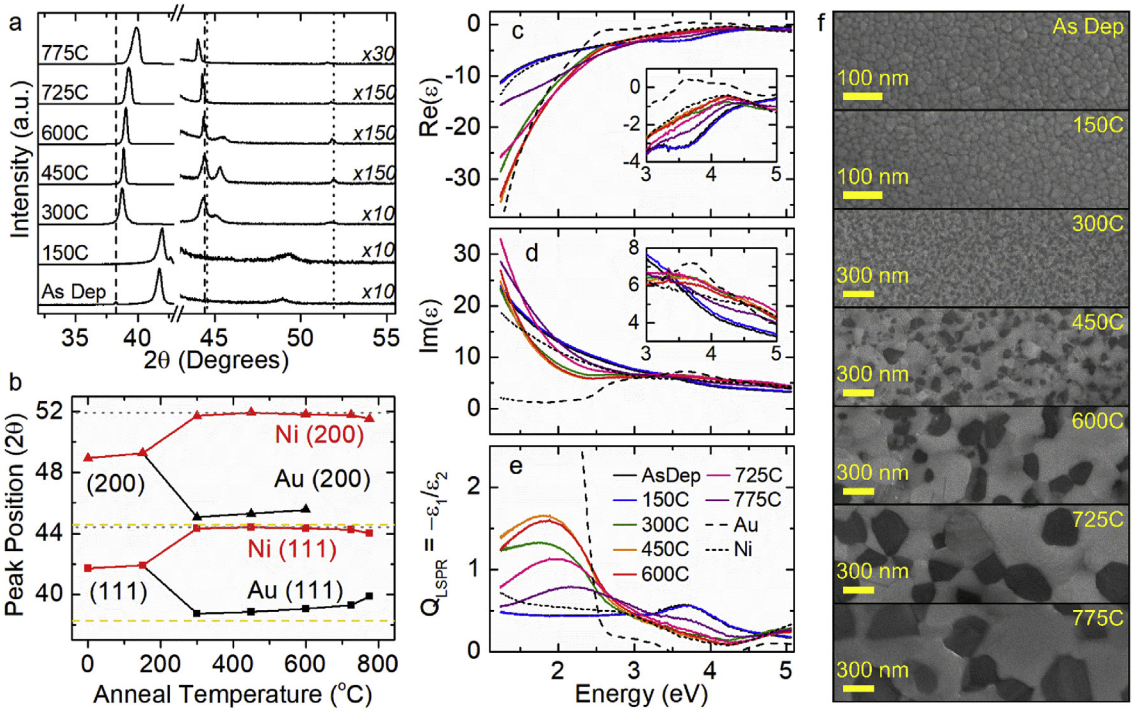

Fig. 5. (a) XRD spectra of $Au_{0.35}Ni_{0.65}$ films for various anneal conditions and (b) corresponding peak positions as a function of temperature demonstrating the shift that occurs with annealing temperature. Real (c) and imaginary (d) components of the dielectric function and corresponding LSPR Q-factor (e). SEM images (f) of $Au_{0.35}Ni_{0.65}$ films for each anneal condition. Dark areas correspond to Ni-rich grains lighter areas are Au-rich grains.

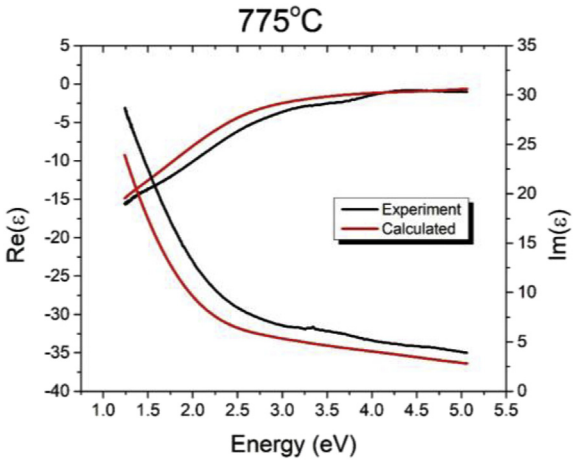

Fig. 6. Experimental (black) and calculated (red) complex dielectric function for an $Au_{0.35}Ni_{0.65}$ alloy after annealing at 775 °C. (For interpretation of the references to colour in this figure legend, the reader is referred to the Web version of this article.)

remaining samples exhibited a gradual shift in the Au-rich (111) peak to higher 2θ, indicating increased Ni content in the Au-rich phase as anneal temperature increased. Concurrently, the Ni-rich (111) peak exhibited a decrease in 2θ with increasing anneal temperature, indicative of increasing Au content. Here, we see there is a larger total shift in the Au peaks than the Ni peaks, which results from the fact that Ni is more soluble in Au than Au is in Ni.

The complex dielectric function and LSPR Q-factor are shown in Fig. 5c–e. Re(ε) behaves similarly to pure Au at lower energies and pure Ni at higher energies. In general, Im(ε) behaves more closely to Ni for the whole spectrum. Again, we utilize the analytical model described above to rationalize the change in the dielectric function; the dielectric functions from each phase are determined by the as-deposited solid solutions and the effective medium approximation used based on the appropriate volume fractions of each phase. Fig. 6 demonstrates the calculated dielectric function for the 775 °C annealed sample compared with the experimental data. Results for other temperatures are shown in Fig. S7. Additionally, the compositions and volume fractions for each temperature are tabulated from the XRD data and summarized in Table S3. The main feature in the Q-factor (~1.8 eV) is similar to that of pure Au but is significantly damped. There are logical shifts in the Q-factor peaks, consistent with the estimated composition of the Au-rich phase; namely the peak shifts gradually to higher energy as the equilibrium composition of the Au-rich phase is enriched in Ni as observed above. The highest Q-factor in the alloy samples comes from the films annealed at 450 °C and 600 °C. Evidently, there is a tradeoff between the Au-rich phase composition and the volume fraction. Higher annealing temperatures promote higher solubilities in the Au-and Ni-rich phases, however the purity and volume fraction of, for instance, the Au-rich phase decreases. Additionally, higher annealing temperatures produced larger grain sizes, as demonstrated in the SEM images of Fig. 5f, which enhance the LSPR due to decreased scattering at grain boundaries.

The phase separation was also observed for 20 nm $Au_{0.50}Ni_{0.50}$ film using a monochromated Carl Zeiss LIBRA 200 MC (S) TEM at an operating voltage of 200 kV equipped with a laser delivery system. Images were collected at 8kX. Selected area electron diffraction patterns (SAED) were collected using a 5 μm aperture and subsequently radially averaged and normalized. The system is described in detail in literature [25]. The as-deposited film was a solid

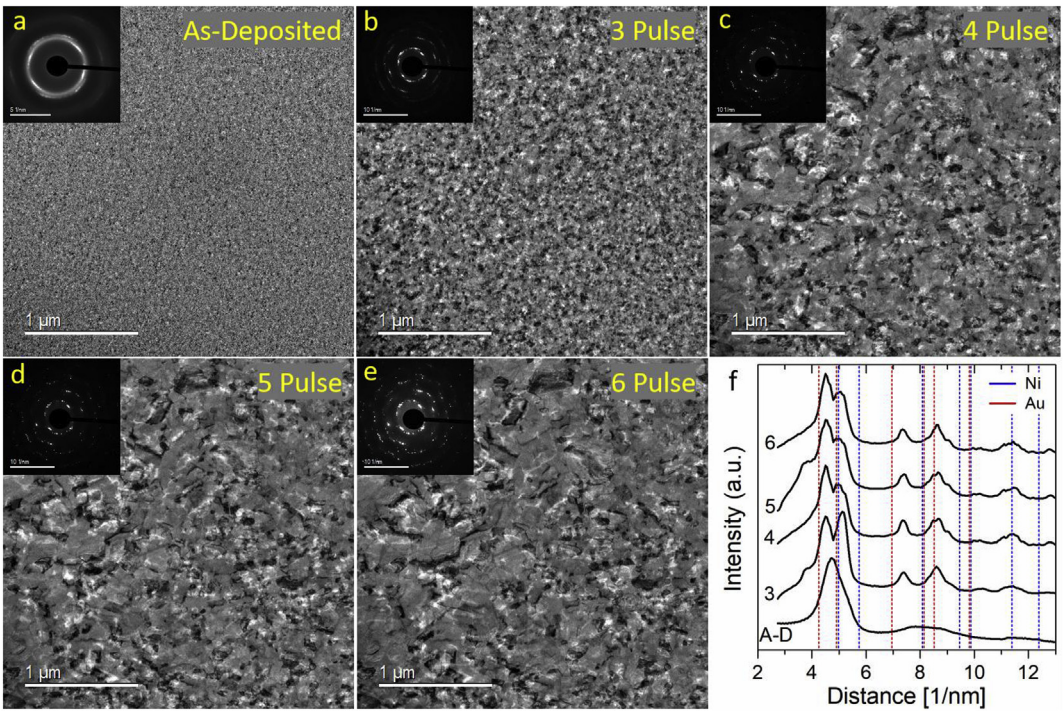

Fig. 7. TEM images and corresponding selected area diffraction patterns (inset) of an $Au_{0.5}Ni_{0.5}$ film in the as-deposited form (a) and after a series of laser pulses (b–e). Radially averaged and normalized SAED patterns for each of the films (a–e), demonstrating that the film is a solid solution in the as-deposited form and phase separation occurs upon annealing.

solution as evidenced by SAED and is shown in Fig. 7a. The film was then photothermally heated *in situ* using a 785 nm wavelength fiber coupled laser delivery system using a series of 200-μs pulses at 13.3 mW. SAED patterns and TEM images were collected after 3, 4, 5, and 6 pulses to observe changes with heating and are shown in Fig. 7b–e. The radially averaged and normalized electron diffraction patterns are shown in Fig. 7f which clearly demonstrates that phase separation occurs after just 3 pulses. See SI for further information.

3.3. $Au_{0.28}Ni_{0.72}$ anneal time dependence study

We were also interested in investigating how annealing time (at 300 °C) affects the dielectric function. Annealing at lower temperatures produces films, which exhibit phase separation into Au-rich and Ni-rich phases with less solubility. Unfortunately, at these temperatures, diffusion is limited and thus phase separation and grain growth occur much more slowly. Additionally, SEM images reveal limited grain coarsening in this time scale (Fig. S9). By further increasing the annealing time, we expect the Q-factor to increase due to the presence of fewer defects in the film and the increased purity of Au-rich grains. Annealing times range from 0.5 to 10 h.

XRD patterns in Fig. 8a reveal the as-deposited film displays two reflections, intermediate to that of pure Au and pure Ni. After the 0.5 h anneal, we already observe phase separation as evidenced by the four peaks that emerge in the XRD, with similar 2θ values to pure Au and pure Ni. However, evidence of the solid solution still remains, although the intensity of the solid solution reflection is greatly reduced. The solid solution (111) reflection is observed in all films except for the film annealed for 10 h. Interestingly, the center of the solid solution reflection generally shifts to higher 2θ values with increasing time, which is characteristic of preferential Au out-diffusion.

The dielectric function, shown in Fig. 8b–d, of the as-deposited film behaves similar to pure Ni in the real component, however, exhibits increased losses in the imaginary component. Annealed samples exhibit very similar dielectric functions. However, upon looking at the Q-factor, we see that an increase in anneal time causes an increase in the Q-factor below 2.5 eV.

4. Conclusions

The dielectric function of $Au_{1-x}Ni_x$ thin film alloys was correlated with the composition and phases present for as-deposited and annealed films. As-deposited films exhibited a supersaturated solid solution across the entire composition range and had a smooth transition in the dielectric function with increasing Ni fraction. The solid solution dielectric functions were modeled using the Drude-critical point model with three critical points. The model parameters were well behaved, and each had a quadratic behavior with composition, allowing us to fit the parameter trends and use them to estimate the dielectric function of intermediate alloys not explicitly measured. Annealed films phase separated into Au- and Ni-rich grains whose compositions depended on the anneal temperature. We demonstrated that the dielectric function of phase separated alloys can be estimated using a composition-weighted average of the Au- and Ni-rich dielectric functions, which were determined using the Drude-3CP model. Additionally, we investigated the temperature and time annealing effects on a fixed alloy composition. With increasing temperature, we observed increased grain growth and decreased purity of the Au-rich and Ni-rich grains. The Q-factor was the largest for 450 °C and 600 °C annealed samples, suggesting there is a trade-off between grain size and composition. By annealing at a low temperature for increasing times, we found that the Q-factor increased. However,

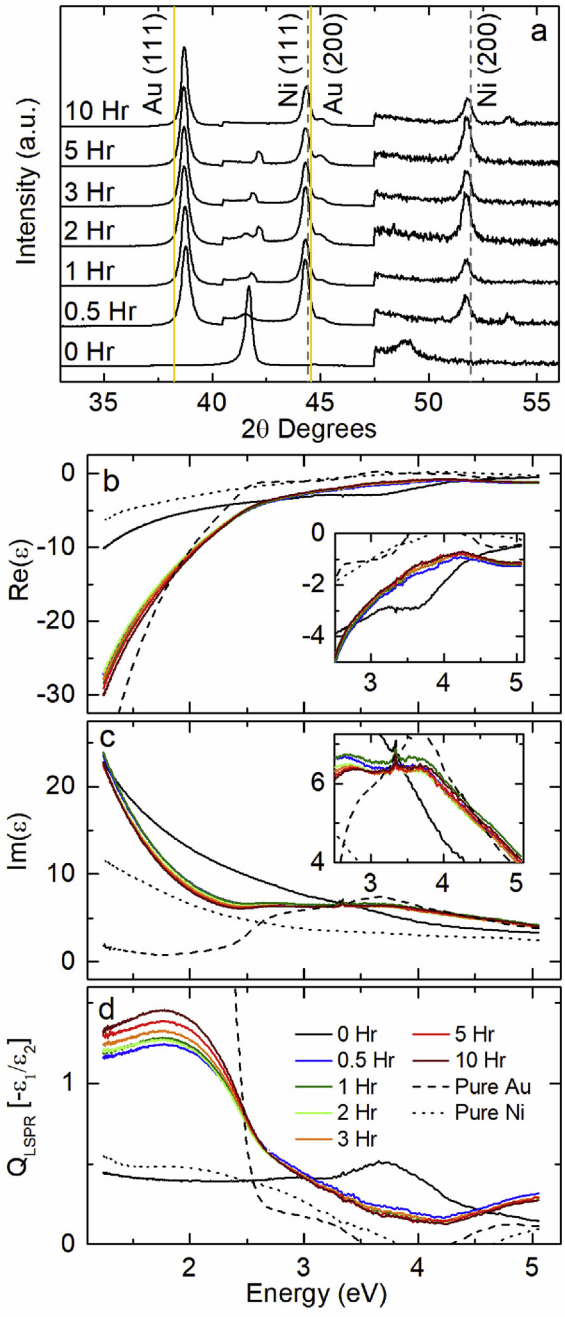

Fig. 8. (a) Grazing x-ray diffraction spectra for $Au_{0.28}Ni_{0.72}$ alloys annealed at various temperatures. The spectra were initially normalized to the largest peak. In the range of 40.5–47.5 2θ, normalized spectra of annealed films are multiplied by a factor of 5. Above 47.5 2θ, normalized spectra are multiplied by a factor of 100. (b–d) Complex dielectric function for annealed $Au_{0.28}Ni_{0.72}$ films and calculated LSPR Q-factor for each annealed film.

longer time scales are needed to fully phase separate the alloy and increase grain size to further enhance the Q-factor.

Acknowledgements

The authors acknowledge support from the National Science Foundation under grant NSF DMR 1709275. X-ray diffraction was performed at the Joint Institute for Advanced Materials (JIAM) Diffraction Facility and Oak Ridge National Laboratory's Center for Nanophase Materials Science. The authors also acknowledge Dr. Kunlun Hong and the Center for Nanophase Materials Sciences, a DOE Office of Science user facility, for use of the spectroscopic ellipsometer.

Appendix A. Supplementary data

Supplementary data to this article can be found online at https://doi.org/10.1016/j.jallcom.2019.04.207.

References

[1] M.G. Blaber, M.D. Arnold, M.J. Ford, A review of the optical properties of alloys and intermetallics for plasmonics, J. Phys. Condens. Matter 22 (2010) 143201. http://stacks.iop.org/0953-8984/22/i=14/a=143201.
[2] V.J. Keast, R.L. Barnett, M.B. Cortie, First principles calculations of the optical and plasmonic response of Au alloys and intermetallic compounds, J. Phys. Condens. Matter 26 (2014) 305501, https://doi.org/10.1088/0953-8984/26/30/305501.
[3] P.R. West, S. Ishii, G.V. Naik, N.K. Emani, V.M. Shalaev, A. Boltasseva, Searching for better plasmonic materials, Laser Photon. Rev. 4 (2010) 795–808, https://doi.org/10.1002/lpor.200900055.
[4] V. Amendola, S. Scaramuzza, S. Agnoli, S. Polizzi, M. Meneghetti, Strong dependence of surface plasmon resonance and surface enhanced Raman scattering on the composition of Au–Fe nanoalloys, Nanoscale 6 (2014) 1423–1433, https://doi.org/10.1039/C3NR04995G.
[5] V. Amendola, M. Meneghetti, O.M. Bakr, P. Riello, S. Polizzi, D.H. Anjum, S. Fiameni, P. Arosio, T. Orlando, C. de Julian Fernandez, F. Pineider, C. Sangregorio, A. Lascialfari, Coexistence of plasmonic and magnetic properties in Au89Fe11 nanoalloys, Nanoscale 5 (2013) 5611–5619, https://doi.org/10.1039/C3NR01119D.
[6] J.T. McKeown, Y. Wu, J.D. Fowlkes, P.D. Rack, G.H. Campbell, Simultaneous in-situ synthesis and characterization of Co@Cu core-shell nanoparticle arrays, Adv. Mater. 27 (2015) 1060–1065, https://doi.org/10.1002/adma.201404374.
[7] H. Garcia, R. Sachan, R. Kalyanaraman, Optical plasmon properties of Co-Ag nanocomposites within the mean-field approximation, Plasmonics 7 (2012) 137–141, https://doi.org/10.1007/s11468-011-9286-4.
[8] R. Sachan, A. Malasi, J. Ge, S. Yadavali, H. Krishna, A. Gangopadhyay, H. Garcia, G. Duscher, R. Kalyanaraman, Ferroplasmons: intense localized surface plasmons in metal-ferromagnetic nanoparticles, ACS Nano 8 (2014) 9790–9798, https://doi.org/10.1021/nn5031719.
[9] G.C. Messina, M.G. Sinatra, V. Bonanni, R. Brescia, A. Alabastri, F. Pineider, G. Campo, C. Sangregorio, G. Li-Destri, G. Sfuncia, G. Marletta, M. Condorelli, R. Proietti Zaccaria, F. De Angelis, G. Compagnini, Tuning the composition of alloy nanoparticles through laser mixing: the role of surface plasmon resonance, J. Phys. Chem. C 120 (2016) 12810–12818, https://doi.org/10.1021/acs.jpcc.6b01465.
[10] E.L. Yates, Xli. Precision measurements of crystal parameters AU - Owen, E.A., London, Edinburgh, Dublin Philos, Mag. J. Sci. 15 (1933) 472–488, https://doi.org/10.1080/14786443309462199.
[11] E.R. Jette, F. Foote, Precision determination of lattice constants, J. Chem. Phys. 3 (1935) 605–616, https://doi.org/10.1063/1.1749562.
[12] J. Wang, X.-G. Lu, B. Sundman, X. Su, Thermodynamic assessment of the Au–Ni system, Calphad 29 (2005) 263–268. https://doi.org/10.1016/j.calphad.2005.09.004.
[13] X. Cen, X. Zhang, A.M. Thron, K. van Benthem, Agglomeration and long-range edge retraction for Au/Ni bilayer films during thermal annealing, Acta Mater. 119 (2016) 167–176. https://doi.org/10.1016/j.actamat.2016.08.021.
[14] M. Bassett, D. Beaglehole, Optical studies of dilute AuNi alloys, J. Phys. F Met. Phys. 6 (1976) 1211–1221, https://doi.org/10.1088/0305-4608/6/6/032.
[15] D.J. McPherson, S. Supansomboon, B. Zwan, V.J. Keast, D.L. Cortie, A. Gentle, A. Dowd, M.B. Cortie, Strategies to control the spectral properties of Au–Ni thin films, Thin Solid Films 551 (2014) 200–204. https://doi.org/10.1016/j.tsf.2013.11.115.
[16] D. Rioux, S. Vallières, S. Besner, P. Muñoz, E. Mazur, M. Meunier, An analytic model for the dielectric function of Au, Ag, and their alloys, Adv. Opt. Mater. 2 (2014) 176–182, https://doi.org/10.1002/adom.201300457.
[17] O. Peña-Rodríguez, Modelling the dielectric function of Au-Ag alloys, J. Alloys Compd. 694 (2017) 857–863. https://doi.org/10.1016/j.jallcom.2016.10.086.
[18] T.J. Kim, T.H. Ghong, Y.D. Kim, D.E. Aspnes, M. V Klein, D.-S. Ko, Y.-W. Kim, V.C. Elarde, J.J. Coleman, Investigation of effective-medium approximation, alloy, average-composition, and graded-composition models for interface analysis by spectroscopic ellipsometry, J. Appl. Phys. 102 (2007) 63512, https://doi.org/10.1063/1.2781519.
[19] S. Link, Z.L. Wang, M.A. El-Sayed, Alloy formation of Gold–Silver nanoparticles and the dependence of the plasmon absorption on their composition, J. Phys. Chem. B 103 (1999) 3529–3533, https://doi.org/10.1021/jp990387w.
[20] M. Gaudry, J. Lermé, E. Cottancin, M. Pellarin, J.-L. Vialle, M. Broyer, B. Prével, M. Treilleux, P. Mélinon, Optical properties of (AuxAg1-x)n clusters embedded in alumina: evolution with size and stoichiometry, Phys. Rev. B 64 (2001) 85407, https://doi.org/10.1103/PhysRevB.64.085407.

[21] P.G. Etchegoin, E.C. Le Ru, M. Meyer, An analytic model for the optical properties of gold, J. Chem. Phys. 125 (2006) 164705, https://doi.org/10.1063/1.2360270.
[22] J. Orosco, C.F.M. Coimbra, On a causal dispersion model for the optical properties of metals, Appl. Opt. 57 (2018) 5333–5347, https://doi.org/10.1364/AO.57.005333.
[23] R. Collette, Y. Wu, A. Olafsson, J.P. Camden, P.D. Rack, Combinatorial thin film sputtering AuxAl1- x alloys: correlating composition and structure with optical properties, ACS Comb. Sci. 20 (2018), https://doi.org/10.1021/acscombsci.8b00091.
[24] R.L. Olmon, B. Slovick, T.W. Johnson, D. Shelton, S.-H. Oh, G.D. Boreman, M.B. Raschke, Optical dielectric function of gold, Phys. Rev. B 86 (2012) 235147, https://doi.org/10.1103/PhysRevB.86.235147.
[25] Y.L. Wu Chenze, Thomas M. Moore, Gregory A. Magel, David A. Garfinkel, Jon P. Camden, Michael G. Stanford, Gerd Duscher, Philip D. Rack, Exploring photothermal pathways via in situ laser heating in the transmission electron microscope: recrystallization, grain growth, phase separation and dewetting in Ag0.5Ni0.5 thin films, Microsc. Microanal. 24 (6) (December 2018) 647–656, https://doi.org/10.1017/S1431927618015465.